

Data-driven Uncertainty Quantification in Computational Human Head Models

Kshitiz Upadhyay^{1,2*}, Dimitris G. Giovanis³, Ahmed Alshareef⁴, Andrew K. Knutsen⁵, Curtis L. Johnson⁶, Aaron Carass⁴, Philip V. Bayly⁷, Michael D. Shields³, K.T. Ramesh^{1,2}

¹Hopkins Extreme Materials Institute, Johns Hopkins University, Baltimore, MD 21218, USA

²Department of Mechanical Engineering, Johns Hopkins University, Baltimore, MD 21218, USA

³Department of Civil and Systems Engineering, Johns Hopkins University, Baltimore, MD 21218, USA

⁴Department of Electrical and Computer Engineering, Johns Hopkins University, Baltimore, MD 21218, USA

⁵Center for Neuroscience and Regenerative Medicine, The Henry M. Jackson Foundation for the Advancement of Military Medicine, Bethesda, MD 20814, USA

⁶Department of Biomedical Engineering, University of Delaware, Newark, DE 19716, USA

⁷Mechanical Engineering and Materials Science, Washington University in St. Louis, St. Louis, MO 63130, USA

Abstract

Computational models of the human head are promising tools for estimating the impact-induced strain response of brain, and thus play an important role in the study and prediction of traumatic brain injury. Modern biofidelic head model simulations are associated with very high computational cost, and high-dimensional inputs and outputs, which limits the applicability of traditional uncertainty quantification (UQ) methods on these systems. In this study, a data-driven manifold learning-based surrogate modeling framework is proposed for UQ of computational head models. This framework is demonstrated on a specific model problem of a 2D subject-specific head model, where the goal is to quantify uncertainty in the simulated strain fields (i.e., output), given the variability in the material properties of different brain substructures (i.e., input). In the first stage of the proposed framework, a data-driven method based on multi-dimensional Gaussian kernel-density estimation and diffusion maps is used to generate realizations of the input random vector of material properties directly from the available data. Computational simulations of a small number of realizations provide input-output pairs for training data-driven surrogate models in the second stage. The surrogate models employ nonlinear dimensionality reduction using Grassmannian diffusion maps to identify a latent representation of the strain fields, Gaussian process regression to create a low-cost mapping between the input random vector and the reduced solution space, and geometric harmonics models for mapping between the reduced space and the Grassmann manifold. It is demonstrated that the surrogate models, even with small training dataset, lead to highly accurate approximations of the computational model while significantly reducing the computational cost. Monte Carlo simulations of the surrogate models are used for uncertainty propagation. UQ of strain fields highlight significant spatial variation in model uncertainty, and reveal key differences in uncertainty among commonly used strain-based brain injury predictor variables.

*Corresponding author: kshitiz@jhu.edu (Kshitiz Upadhyay)

Keywords

Head injury model; Traumatic Brain Injury (TBI); Surrogate model; Grassmann manifold; Gaussian process regression; Diffusion maps; Uncertainty quantification

1. Introduction

Traumatic brain injuries (TBIs) are one of the leading causes of mortality and morbidity in the world, with the latest data from United States showing nearly 61,000 TBI-related fatalities in 2019 [1]. Caused by the rapid application of external forces on the head, TBI can lead to a host of disabilities: lost or impaired consciousness, memory loss, confusion, disorientation, altered vision, weakness etc. [2,3]. Due to the mechanical origins of TBI, biofidelic computational head models have been extensively used to study the strain-response of brain under rapid loading conditions, which has been correlated to the risk of brain injury[4–6]. In this way, computational head models are playing a critical role in bridging the gap between external mechanical insult to the head and the resulting neurological pathology.

A computational head model is composed of three basic constituents: head geometry, material properties, and boundary conditions. Each of these input parameters are associated with considerable variability. For example, a study [7] on the brain volume of 52 healthy humans (both males and females) found a size difference of ~81% between the largest and the smallest brains. Similar differences are also seen in the case of the material properties input. For example, between three experimental studies [8–10] in the literature, the reported long-term shear modulus of brain varies between 12.6 Pa to 303.3 Pa. A few recent studies have shown that variability in head shape/size and brain tissue material properties can lead to very different simulated strain responses from head models [11,12]. Such discrepancy in reported strains can lead to very different injury risk predictions, which diminishes the applicability of these head models in real-world injury scenarios. Despite this, a majority of the available human head models are developed using deterministic inputs of “average” head geometry (e.g., from a 50-percentile male [13]), material properties and boundary conditions, and the uncertainty quantification (UQ) of these models has received little attention.

UQ of computational head models is associated with significant challenges. For instance, a typical forward uncertainty propagation requires running large number of simulations with different realizations of input parameters (as a random vector). As high fidelity computational head model simulations, which feature nonlinear constitutive models and complex geometrical features, generally run for hours to days [14,15], their UQ becomes prohibitively expensive. Surrogate models can alleviate this issue to an extent by providing a low-cost approximation of the computational model. However, creating accurate surrogate models with a small number of available training data due to limited number of feasible computational model runs is non-trivial, and requires careful sampling of realizations from the input parameter space. Further, complex biofidelic head models are associated with high dimensional inputs and outputs; for example, a typical finite element head simulation results in a strain field at tens of thousands of nodes [15]. Such a high dimensionality of model inputs and outputs can lead to poor accuracy of the surrogate model, and issues such as the curse of dimensionality and over-fitting [16,17]. Due to these challenges, existing studies on the UQ of head models in the brain biomechanics community have only focused on low-fidelity, low-dimensional head models [18–21].

In this study, a data-driven manifold learning-based surrogate modeling framework is proposed for UQ of high-fidelity, high-dimensional computational human head models. For this, a 2D subject-specific human head model of a 31-year-old male subject is selected as a model problem, in which anatomically accurate head geometry is derived from magnetic resonance imaging (MRI) and susceptibility-weighted imaging (SWI), while the nonlinear visco-hyperelastic material parameters of different brain regions are derived using magnetic resonance elastography (MRE). While head geometry and boundary conditions (mild rotational acceleration of the head) are assumed to be deterministic, the material parameters within individual brain regions can significantly vary. The objective is to study the effect of this variability on two time-independent scalar strain fields: maximum axonal strain (MAS) and cumulative maximum principal strain (CMPS). In the first stage of the proposed UQ framework, the probabilistic sampling method introduced in [22] is utilized to generate realizations of the high-dimensional (input) random vector (containing the material properties) based on the available experimental MRE data. In the second stage, a surrogate model is trained to create a low-cost and accurate mapping between the material properties and the MAS/CMPS fields. The surrogate model employs manifold learning (e.g., Grassmannian diffusion maps [23]) to identify a latent representation of the MAS/CMPS fields, and machine learning (e.g., Gaussian process [24], geometric harmonics [25]) to create a mapping between (i) the input random vector and the reduced solution space and, (ii) the reduced space and the Grassmann manifold. The proposed framework accelerates the UQ of the full MAS/CMPS fields, given the uncertainty in the head model material properties.

The paper is organized as follows: Section 2 describes the 2D subject-specific computational head model and its associated uncertainties. In Section 3, the proposed data-driven UQ framework is formalized, and the surrogate model is trained to create a mapping between the MRE material properties and the full-field strain maps. Section 4 discusses the performance of the proposed surrogate in predicting the full strain fields. The uncertainty in the predicted strain fields and in a number of scalar strain measures commonly employed for the quantification of brain injury, are reported.

2. Subject-Specific 2D Head Model

In a recent study by the authors [26], a subject-specific 3D head model was developed for a healthy 31-year-old male subject (illustrated in Fig. 1), using head geometry derived from magnetic resonance imaging (MRI) and susceptibility weighted imaging (SWI), and visco-hyperelastic material properties calibrated from in-vivo magnetic resonance elastography [27,28] (MRE). This model was employed to simulate brain deformation under mild rotational accelerations to the head about the inferior-superior (z-) axis, using a meshless, material point method (MPM) numerical technique. The simulation results were validated using experimentally observed time-varying strain fields under the same loading condition acquired via tagged MRI (tMRI) of a neck rotation experiment [29], conducted on the same human subject. In this work, a 2D version of this validated 3D head model (see Fig. 1(g)) is selected in order to quantify uncertainty in the strain fields resulting from the simulation of neck rotation motion, given the uncertainty in the input material properties. Note that 2D head simulations of this loading condition are common in the literature because of the nearly planar deformation fields (i.e., negligible out-of-axial plane motion in the z-direction) [30,31].

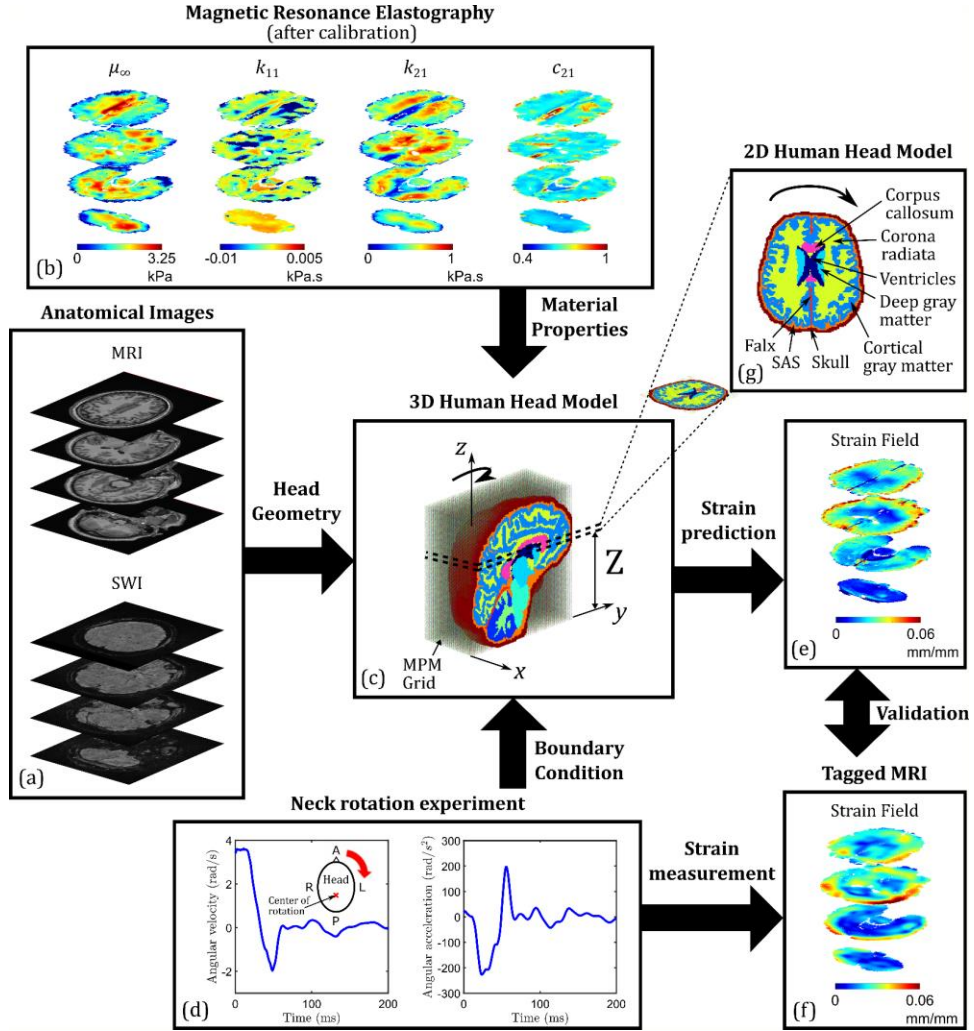


Figure 1. Flowchart of the development of subject-specific computational human head models. (a) Segmented and processed anatomical images from MRI (T1- and T2-weighted) and SWI provide the 3D head geometry, while (b) in-vivo MRE is used to calibrate nonlinear visco-hyperelastic material properties of major brain substructures. (c) The resulting MPM-based 3D head model is used to simulate a (d) neck rotation experiment. (f) Tagged MRI of this experiment yields full-field strain data for model validation. In this study, a (g) 2D slice of the 3D head model is considered for UQ purposes.

Different aspects of the subject-specific 2D head model will now be discussed in a greater detail. The first subsection discusses the measurement of full-field strain response under neck rotation using tMRI, which dictates the choice of the axial layer for 2D model development (i.e., the distance Z in Fig. 1(c)). The second subsection briefly discusses the geometry and brain morphometry of the 2D head model along with the constitutive modeling and numerical simulation frameworks (for details, refer to the original 3D model article). Finally, the last subsection describes the uncertainties associated with the 2D head model, which serve as a motivation for this work.

2.1. Tagged MRI and the choice of axial brain layer

As mentioned before, tMRI was employed in Upadhyay et al. [26] to obtain full-field 3D displacements and strain fields from neck rotation experiments (see experimental details in Knutsen et al. [29]) on a 31-year-old human subject (Fig. 1(d),(f)). In this experiment, a controlled non-injurious impulsive loading is applied on the subject's head, which rotates in the axial plane about the inferior-superior (I/S) axis (center of rotation roughly passes through the brain stem). The loading input to the head is measured using an angular position sensor, which also provides boundary condition to the computational model. Figure 1(d) shows the angular velocity and acceleration versus time plots. Time-varying Green-Lagrange (G-L) strain tensor fields during this loading condition are measured at a spatial resolution of 1.5 mm (isotropic) and a temporal resolution of 18 ms, using tMRI. These tensorial strain fields are generally reduced to two scalar strain measures during post-processing: (i) maximum principal strain, MPS (first principal eigenvalue of the G-L strain tensor), and (ii) axonal strain, E_f . The latter is computed as,

$$E_f = \mathbf{a}_0 \cdot \mathbf{E} \cdot \mathbf{a}_0 \quad (1)$$

where \mathbf{a}_0 is the axonal fiber direction at a given brain voxel obtained from Diffusion Tensor Imaging (DTI), and \mathbf{E} is the G-L strain tensor yielded by tMRI. It is important to note that while MPS is computed for the entire brain volume, E_f is only computed for brain voxels in the anisotropic white matter regions (i.e., corpus callosum, corona radiata, cerebellar white matter, and brainstem), with a fiber anisotropy (FA) value of greater than or equal to 0.2 (FA field is also obtained from DTI). This is a standard criterion [32] that is implemented to exclude regions of isotropic diffusion such as gray matter and cerebrospinal fluid.

The experimentally observed strain-response of brain can be indicative of its vulnerability to injuries such as diffuse axonal injury (DAI) [29]: higher values of scalar strain measures at a given location in brain are generally considered synonymous to a greater probability of injury. As a result, the cumulative MPS (CMPS) and maximum axonal strain (MAS), which are the peak values of MPS and E_f at a given brain voxel over the entire loading duration, respectively, are commonly used as metrics for the quantification of brain injury [4–6,33]. Note that both CMPS and MAS are time-independent scalar strain measures. In this study, the axial layer of brain in which the greatest area fraction is associated with MAS greater than the 50- and 95-percentile MAS thresholds evaluated over the entire 3D brain volume, is selected for 2D head model development. This brain layer is considered as the most vulnerable to injury.

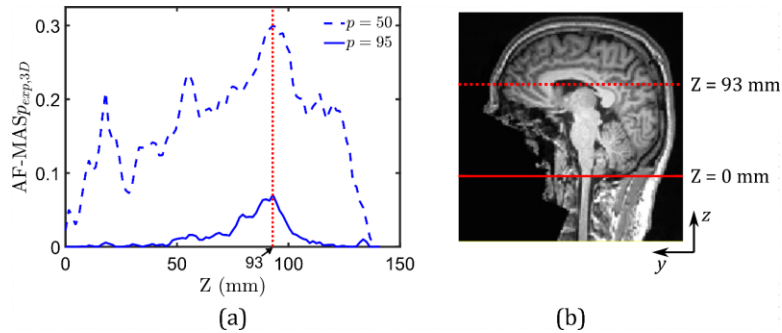


Figure 2. (a) Area fractions of the axial layers/slices of brain where MAS is greater than the global 50- and 95-percentile MAS thresholds, as a function of their position in the z-direction (along the Inferior-Superior axis). A generic MAS area fraction-based metric for p^{th} percentile MAS threshold is denoted by AF-MAS $p_{exp,3D}$. (b) T1-weighted MRI image of the midsagittal (yz-) plane, showing the position of axial layers at Z = 0 and 93 mm.

Figure 2(a) plots the area fractions of different axial layers exposed to MAS greater than the 50- (dashed line) and 95-percentile (solid line) MAS thresholds as a function of their z-location. Note, $Z = 0$ mm, indicated on the midsagittal slice of T1-weighted MRI image in Fig. 2(b), corresponds to the bottom-most brain voxel (excluding SAS and skull) in the 3D head model in Fig. 1(c). Both the 50- and 95-percentile MAS area fraction-based metrics reach maxima at $Z = 93$ mm. Thus, this particular axial layer/slice, which passes through the genu of corpus callosum, is chosen for the 2D head model development in this work.

Finally, full-field 3D displacements observed from tMRI are also used to verify the assumption of zero out-of-plane displacement of material points in the 2D head model. For this, the observed average z-displacement of the $Z = 93$ mm layer from tMRI is compared with the corresponding x- and y-displacements. It is found that the average z-displacement is only $\sim 10\%$ of the average x- and y-displacements, which provides a reasonable justification for the zero z-displacement constraint in the 2D model simulations.

2.2. Model development

In Upadhyay et al. [26], subject-specific 3D anatomical images of the subject head were acquired using MRI and SWI were processed and segmented into multiple smaller substructures: deep gray matter, cortical gray matter, corona radiata, corpus callosum, cerebellum gray matter, cerebellum white matter, brainstem, ventricles, cerebrospinal fluid (CSF), falx, tentorium, and subarachnoid space (SAS). An “artificial” skull was then added to create the 3D head geometry (spatial resolution: 1.5 mm isotropic) for simulations. In this study, a single axial slice of this 3D geometry (Fig. 1(c)), corresponding to $Z = 93$ mm, is used as 2D head model geometry for neck rotation simulation. Note that data from all the biomedical imaging techniques (MRI, SWI, MRE and tMRI) was in a common coordinate space, allowing a one-to-one correspondence of brain voxel locations between geometry, material properties, and experimental strain fields. There are eight substructures in the 2D head model (see Fig. 1(g)): deep gray matter, cortical gray matter, corona radiata, corpus callosum, ventricles, falx, SAS, and skull.

In-vivo MRE was conducted on the same human subject in Upadhyay et al. [26] to acquire spatially resolved full-field maps of the storage modulus and loss modulus at three actuation frequencies (i.e., 30, 50 and 70 Hz). Due to its coarse resolution (i.e., 1.5 mm isotropic), MRE maps only consist of the four major, parenchymal brain substructures: deep gray matter, cortical gray matter, corona radiata, corpus callosum. The frequency-dependent storage and loss moduli at every MRE brain voxel are combined with stress-strain data from ex-vivo experiments on human brain tissues to calibrate a nonlinear visco-hyperelastic Ogden-Upadhyay-Subhash-Spearot (O-USS) constitutive model [34] (see details of the calibration procedure in Upadhyay et al. [26]). A brief description of the O-USS model is provided in the supplementary material. It consists of six model parameters: μ_∞ – long-term shear modulus, α – compression-tension asymmetry parameter, k_{11} – linear rate sensitivity control parameter, k_{21} – nonlinear rate sensitivity control parameter, c_{11} – rate sensitivity index, and κ – bulk modulus.

The calibration of full-field visco-hyperelastic material properties from MRE and the subsequent consideration of a single axial layer at $Z = 93$ mm yields four O-USS model parameters, viz., μ_∞ , k_{11} , k_{21} , and c_{21} , for every voxel in the deep gray matter, cortical gray matter, corona radiata, and corpus callosum substructures of the 2D head model. Note that the parameter α , which captures the nonlinearity in the quasi-static stress-strain response under large deformations, cannot be calibrated from in-vivo MRE because MRE

probes the material only in its small deformation regime. Similarly, bulk modulus κ also cannot be obtained from MRE, which assumes incompressibility of material response. Therefore, while α is directly calibrated for each of the four major substructures from their ex-vivo stress versus strain responses from the literature, a constant value of κ for brain tissue is taken from the literature. Finally, material properties of the finer brain substructures that were unresolved in MRE (i.e., SAS, falx, skull, and ventricles) are taken directly from ex-vivo experimental data in the literature. Among these minor regions, SAS is modeled as a soft linear viscoelastic (LVE) solid characterized by a short-term shear modulus G_0 , fitting parameter g_1 and time-constant τ_1 , while falx and skull are modeled as linear elastic solids characterized by a Young's modulus E and a Poisson's ratio ν . Ventricles are modeled as a viscous fluid using shear viscosity μ and the parameter n of the Murnaghan-Tait equation of state [35]. For more details on these constitutive formulations, refer the original 3D model development article [26]. The average (mean) material properties of all the eight substructures of the 2D head model are listed in Table 1.

Table 1. Average material properties of the various substructures of the 2D head model employed in this work.

Brain substructure	Material properties (O-USS model)						
	μ_{∞} (kPa)	α	k_{11} (kPa.s)	k_{21} (kPa.s)	c_{21}	κ (GPa)	ρ (kg/m ³)
Deep gray matter	1.10	4.92	-0.152	0.584	0.879	2.19	1040
Cortical gray matter	1.35	-3.76	-0.461E-2	0.441	0.672		
Corpus Callosum	2.11	-2.32	-0.224E-2	0.517	0.598		
Corona Radiata	1.73	-3.47	-0.343E-2	0.635	0.635		
	Material properties (LVE model)						
	G_0 (kPa)	g_1	τ_1 (ms)	κ (GPa)	ρ (kg/m ³)	Reference	
Sub-arachnoid space	0.5	0.8	12.5	2.19	1133	Mao et al. (2013) [36]	
	Material properties (Linear elastic model)						
	E (MPa)	ν	ρ (kg/m ³)	Reference			
Falx	31.5	0.45	1133	Galford and McElhaney (1970) [37]			
Skull	8000	0.22	2070	McElhaney (1973) [38]			
	Material properties (Fluid model)						
	μ (Pa.s)	n	ρ (kg/m ³)	Reference			
Ventricles	1.002e-3	7.15	1004	Goldsmith (1970) [39]			

Finally, the 2D subject-specific head model is used to simulate mild rotational acceleration (Fig. 1(d)) of the head over a 189 ms duration, using the Uintah software MPM package (see simulation details in Upadhyay et al. [26]). The simulation results in the time-varying full-field G-L strain maps of 2D brain at a spatial resolution of 1.5 mm, and a temporal resolution of 3 ms. The tensorial G-L strain is used to compute the time-independent scalar strain fields of MAS and CMPS during post-processing. Plots showing the

comparison of the simulated strain-response from the head model employing mean material properties (Table 1) with corresponding observed strain-response from tMRI, are shown in the supplementary material. A good agreement is observed both in terms of the magnitudes (evaluated at 95-percentile) of strain measures, E , E_f and MPS, and their evolution in time. Thus, the 2D subject-specific head model considered in this study is a validated model.

2.3. Source of uncertainty in the 2D head model

In order to set up and run a simulation of the subject-specific 2D computational head model in Fig. 1(g), model geometry, material properties, and boundary conditions have to be specified. In the present setting, both the head geometry, which is derived directly from anatomical images of the subject's head, and boundary condition, which is directly measured using an angular position sensor during the neck rotation experiment, are considered to be deterministic. However, material properties that are assigned to each of the brain substructures constitute a significant source of uncertainty, which affects the model output (e.g., simulated strain fields). Figure 3(a) shows box plots of the four visco-hyperelastic material properties derived from in-vivo MRE for each of the four major substructures of the 2D model (note, each substructure is composed of a number of brain voxels, each with one set of material properties). Significant inter-region variability of these material properties is evident from these plots. To highlight the effect of this variability on the simulated response, Fig. 3(b) compares the MAS and CMPS strain fields of the head model for two different sets of material properties values: mean (Table 1) and randomly sampled, assigned to each of the four brain regions (both sets are highlighted on the box plots). From this figure, in the case of randomly sampled material properties, the simulation gives larger overall strain values compared to the mean material properties case. Quantitatively, the 50- and 95-percentile MAS of the former simulation are 0.011 mm/mm and 0.037 mm/mm, respectively, which is 66.67% and 12.12% higher compared to the mean material properties case; similarly, the 50- and 95-percentile CMPS are 14.85% and 17.10% higher. The goal of the present study is thus to quantify uncertainty in the strain output of the subject-specific 2D head model originating from the variability in material properties of brain substructures. Specifically, MAS and CMPS strain field outputs are considered.

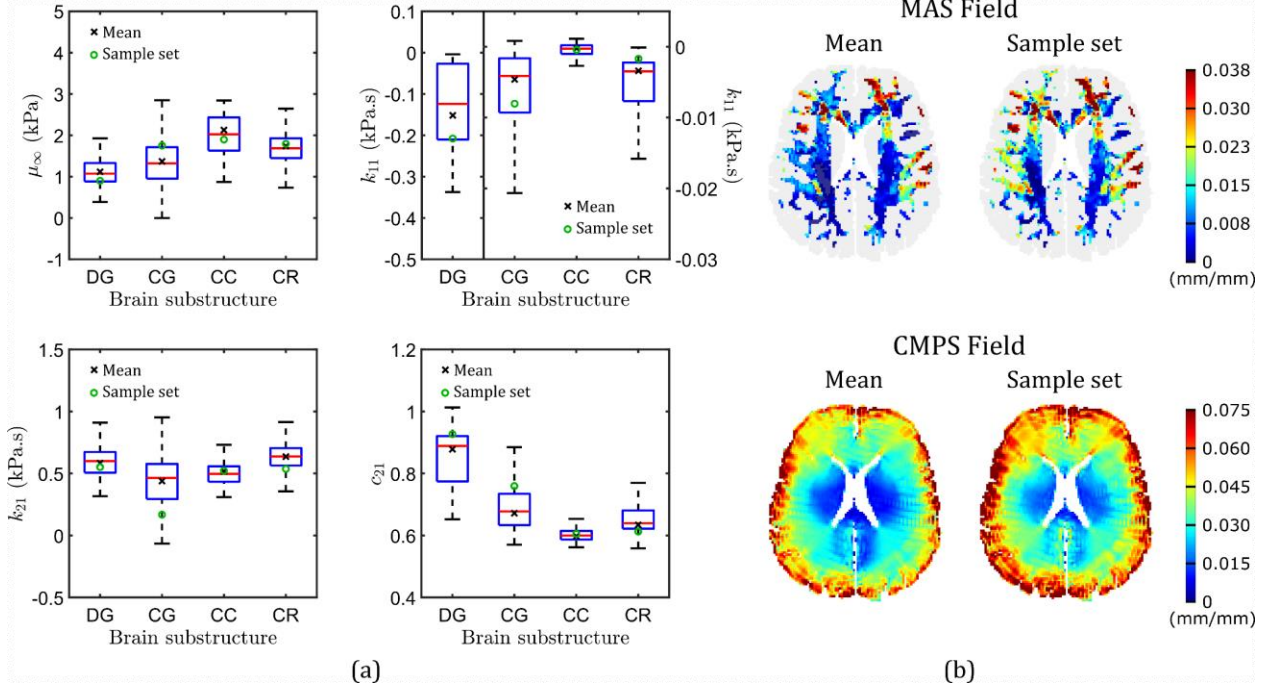


Figure 3. (a) Box plots of the four visco-hyperelastic material properties calibrated for brain voxels in the four major brain substructures: deep gray matter (DG), cerebrum gray matter (CG), corpus callosum (CC) and corona radiata (CR). On each of the boxes, the central red line indicates the median, and the bottom and top edges indicate the 25th and 75th percentiles, respectively. Maximum whisker length is 1.5 times the interquartile range. (b) Comparison of MAS and CMPS strain fields simulated by two head models: one based on mean material properties, and the other based on a randomly sampled set of properties.

3. Proposed Uncertainty Quantification framework

3.1. Problem statement

Consider a complete probability space $[\Omega, F, P]$, where Ω is the sample space, $F \subset 2^{\Omega}$ is the σ -algebra of the events and P is the probability measure. Furthermore, let $\mathbf{X}(\omega) = \{X_1(\omega_1), \dots, X_n(\omega_n)\} \in X \subset \mathbb{R}^n$ denote a vector of n random variables having probability density function (pdf) $f_X(\mathbf{x})$, indexed on $\omega = \{\omega_1, \dots, \omega_n\} \in \Omega = [0, 1]^n$. The stochastic formulation of the present problem is defined as

$$\mathcal{M}^{(\text{MAS}, \text{CMPS})}(\mathbf{X}_{\mathbf{M}}(\omega)) = \mathbf{Y}_{\mathbf{M}}^{(\text{MAS}, \text{CMPS})} \quad (2)$$

where $\mathcal{M}(\cdot)$ is the 2D head model, $\mathbf{X}_{\mathbf{M}}(\omega)$ is the vector containing the material parameters and \mathcal{M}^{MAS} and $\mathcal{M}^{\text{CMPS}}$ represent mappings to the random vectors of the output MAS and CMPS fields, $\mathbf{Y}_{\mathbf{M}}^{\text{MAS}}$ and $\mathbf{Y}_{\mathbf{M}}^{\text{CMPS}}$, respectively. For the 2D subject-specific head model, vector $\mathbf{X}_{\mathbf{M}} \in \mathbb{R}^{16}$ (ω is omitted for the remaining of the paper) consists of the four visco-hyperelastic material properties (i.e., μ_{∞} , k_{11} , k_{21} , and c_{21}) for all four brain substructures (i.e., deep gray matter (DG), cortical gray matter (CG), corona radiata (CR), and corpus callosum (CC)), derived from in-vivo MRE:

$$\mathbf{X}_{\mathbf{M}} = (\mu_{\infty}^{\text{DG}}, k_{11}^{\text{DG}}, k_{21}^{\text{DG}}, c_{21}^{\text{DG}}, \mu_{\infty}^{\text{CG}}, k_{11}^{\text{CG}}, k_{21}^{\text{CG}}, c_{21}^{\text{CG}}, \mu_{\infty}^{\text{CR}}, k_{11}^{\text{CR}}, k_{21}^{\text{CR}}, c_{21}^{\text{CR}}, \mu_{\infty}^{\text{CC}}, k_{11}^{\text{CC}}, k_{21}^{\text{CC}}, c_{21}^{\text{CC}}) \in \mathbb{R}^{16} \quad (3)$$

The output random vector $\mathbf{Y}_M^{\text{MAS}} \in \mathbb{R}^{2125}$ consists of MAS values at brain voxels in the structurally anisotropic white matter regions (i.e., corona radiata and corpus callosum). On the other hand, $\mathbf{Y}_M^{\text{CMPS}} \in \mathbb{R}^{6372}$ consists of brain voxels in all four brain substructures, and thus is a larger vector compared to $\mathbf{Y}_M^{\text{MAS}}$. Every component in these two vectors corresponds to a specific voxel in the 2D brain.

In order to perform UQ, it is necessary to draw samples from the joint pdf $f_{\mathbf{X}_M}(\mathbf{x})$ of \mathbf{X}_M and run the computational model $\mathcal{M}(\cdot)$. However, this joint pdf is not known a-priori. To this end, the data-driven methodology introduced in [22] is utilized in this study to sample realizations of \mathbf{X}_M that are statistically consistent with the available in-vivo MRE data. This process is described in the Section 3.2. Once a large number of realizations of the input random vector \mathbf{X}_M are generated, uncertainty can be propagated through the model $\mathcal{M}(\cdot)$ in order to calculate the statistical properties of the MAS and CMPS strain field outputs, respectively. However, due to the excessive computational cost of running computational head models (for instance, a single 2D subject-specific head model simulation runs for several hours on a supercomputing cluster), propagation of uncertainty directly via $\mathcal{M}(\cdot)$ is not feasible.

To overcome this bottleneck, the present study proposes development of a surrogate model $\tilde{\mathcal{M}} \equiv \mathcal{M}(\cdot)$ that will reasonably mimic the strain response of the computational head model (i.e., $\tilde{\mathcal{M}}(\mathbf{X}_M) \approx \mathcal{M}(\mathbf{X}_M)$) in a fraction of the computational time required by the model $\mathcal{M}(\cdot)$. In order to create the training data, the computationally expensive 2D head model is run for a small number of \mathbf{X}_M realizations that span the probability space efficiently. Once trained, the surrogate will be used in the framework of Monte Carlo simulation to predict the MAS and CMPS fields and calculate their statistical properties. The details of the surrogate model are discussed in Section 3.3.

3.2. Data-driven sampling

The data-driven methodology introduced in [22] is employed to generate realizations of the random vector \mathbf{X}_M that are statistically consistent with available in-vivo MRE data. Briefly, the method utilizes a multi-dimensional Gaussian kernel-density estimation to obtain the probability distribution of the scaled and normalized data. Then, diffusion maps is used to reveal the local geometry of the subset $\mathcal{S} \subset \mathbb{R}^{16}$ on which the probability distribution is concentrated. Diffusion maps require choosing a Gaussian kernel smoothing parameter (ε) and a parameter κ that is used to fix the analysis scale of the local geometric structure of the dataset (refer [22] for details). Finally, Markov Chain Monte Carlo (MCMC) based on Itô stochastic differential equations is utilized to sample realizations of the random vector that are confined in \mathcal{S} . However, for the 2D head model, one challenge is that the in-vivo MRE data are, in some sense, heterogeneous; one set of material properties is available per brain voxel, but the number voxels in the four brain substructures is different. To overcome this, the present study proposes a two-step strategy for generating data for the entire 2D head model that are consistent with the available in-vivo MRE data:

Step 1: For each one of the four individual substructures, generate realizations of the random vector $\mathbf{X}_M^i \in \mathbb{R}^4$:

$$\mathbf{X}_M^i = (\mu_{\infty}^i, k_{11}^i, k_{21}^i, c_{21}^i) \quad (4)$$

where $i \in \{\text{DG}, \text{CG}, \text{CR}, \text{CC}\}$. In this case, the in-vivo MRE data in each one of the brain substructures, used to drive the sampling, consist of 300 points randomly selected from the material properties. 600 additional

realizations are generated using the data-driven method and 100 realizations (out of a total of 900) are randomly selected to represent substructure i . By definition, data $D_i \in \mathbb{R}^{4 \times 100}$ are statistically consistent with the in-vivo MRE data for the brain substructure i .

Step 2: Combine data D_i from all brain substructures in order to create a dataset $D \in \mathbb{R}^{16 \times 100}$ to drive the generation of realizations of the random vector $\mathbf{X}_M \in \mathbb{R}^{16}$ that contain the material properties for the entire 2D head model. Having identified dataset D that is “implicitly” consistent with MRE data, 10200 additional realizations of \mathbf{X}_M are then generated (i^{th} realization is denoted by $\mathbf{x}_M^{(i)}$). Out of the total 10300 realizations, 300 are used as the training set for the surrogate model (presented next) and 10000 are used for performing Monte Carlo simulations using the trained surrogate.

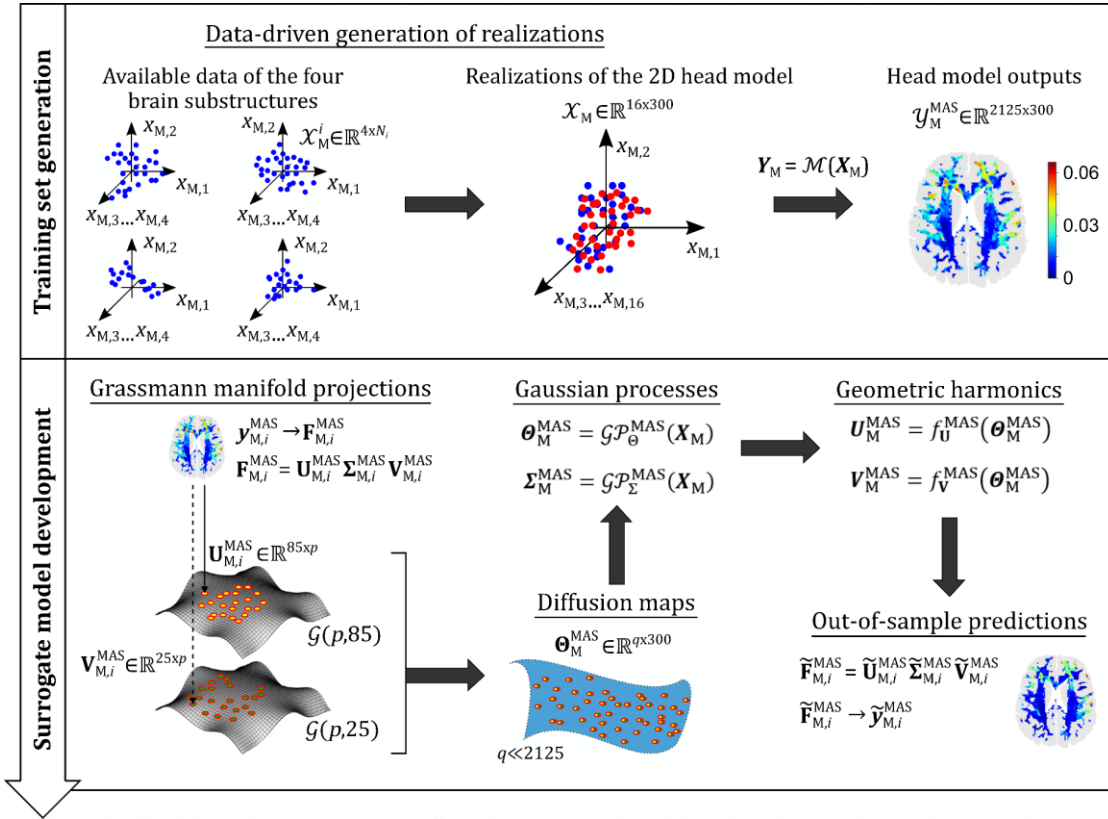


Figure 4. A schematic illustration of the proposed data-driven surrogate modeling framework for UQ of computational head models: in the first stage, the available material properties of each of the four substructures, $\mathbf{x}_M^i \in \mathbb{R}^{4 \times N_i}$ (N_i denotes number of voxels for substructure i) are used to generate 300 realizations of the input random vector of material properties for the 2D head model (i.e., \mathbf{X}_M). Simulations of these realizations yields input-output ($\mathbf{Y}_M^{\text{MAS}}$) data set for training the surrogate model in the second stage. Surrogate model is developed in three steps: first step performs nonlinear dimensionality reduction on the output via Grassmannian diffusion maps, second step creates Gaussian process mappings between input and reduced solutions (i.e., $\boldsymbol{\theta}_M^{\text{MAS}}$ and $\boldsymbol{\Sigma}_M^{\text{MAS}}$), and the third step allows out-of-sample predictions by mapping diffusion coordinates $\boldsymbol{\theta}_M^{\text{MAS}}$ to orthogonal matrices $\mathbf{U}_M^{\text{MAS}}$ and $\mathbf{V}_M^{\text{MAS}}$ of the Grassmann manifold via geometric harmonics, followed by reverse SVD.

3.3. Surrogate modeling

Having obtained a set of 300 realizations of the input random vector i.e., $\mathcal{X}_M = \{\mathbf{x}_M^{(1)}, \mathbf{x}_M^{(2)}, \dots, \mathbf{x}_M^{(300)}\}$, the 2D subject-specific computational head model is run in order to compute the corresponding model output solutions, $\mathcal{Y}_M^{\text{MAS}} = \{\mathbf{y}_{M,1}^{\text{MAS}}, \mathbf{y}_{M,2}^{\text{MAS}}, \dots, \mathbf{y}_{M,300}^{\text{MAS}}\}$ and $\mathcal{Y}_M^{\text{CMPS}} = \{\mathbf{y}_{M,1}^{\text{CMPS}}, \mathbf{y}_{M,2}^{\text{CMPS}}, \dots, \mathbf{y}_{M,300}^{\text{CMPS}}\}$, where $\mathbf{y}_{M,i}^{\text{MAS}}$ and $\mathbf{y}_{M,i}^{\text{CMPS}}, i = 1, \dots, 300$, are vectors containing 2125 MAS and 6372 CMPS values, respectively. The goal is now to train two surrogate models using this available input-output data that will map the high-dimensional (\mathbb{R}^{16}) input to the very high-dimensional output space of MAS (\mathbb{R}^{2125}) and CMPS (\mathbb{R}^{6372}) fields. Two major challenges in this regard are the availability of only a small number of training data (due to high cost of the computational head model) and the very high-dimensionality of the outputs, both of which lead to poor accuracy of surrogate models in performing out-of-sample predictions (which is required for UQ). To overcome these challenges, a recently proposed manifold learning-based surrogate framework [40] is employed in this work for developing data-driven surrogate models on very high-dimensional outputs of the computational head models.

The following two subsections demonstrate the construction of the surrogate model, which is performed via three steps (see Fig. 4): (i) the very high-dimensional solution space is embedded onto low-dimensional Grassmannian diffusion manifold, (ii) a Gaussian process surrogate is trained to map the input space to the low-dimensional solution space, and (iii) the predicted low-dimensional reduced solutions are expanded via geometric harmonics models to reconstruct full, very high-dimensional solutions. It is important to note that in the original framework [40], a Polynomial Chaos expansion (PCE) was used to create the mapping from the input to the reduced space. However, since PCE suffers from the curse of dimensionality (i.e., exponential growth of the number of unknown coefficients with the input dimension), and in the 2D head model, the input space is high dimensional (16 dimensions), Gaussian process regression is selected as the tool to perform the mapping [24]. Note, several other machine learning methods can also be used for this purpose, such as geometric harmonics [25] and artificial neural networks [41]. For clarity, only the MAS strain field output is considered in the following description; the same procedure is followed for building the surrogate model for mapping input to the CMPS strain field.

3.3.1. Step I

In the first step, the very high-dimensional output data is projected onto a low-dimensional space using Grassmannian diffusion maps [23]. For this, each output is first reshaped into matrix form (i.e., $\{\mathbf{y}_{M,i}^{\text{MAS}} \in \mathbb{R}^{2125}\}_{i=1}^{300} \rightarrow \{\mathbf{F}_{M,i}^{\text{MAS}} \in \mathbb{R}^{85 \times 25}\}_{i=1}^{300}$), and then, linearly projected onto a Grassmann manifold by means of thin singular value decompositions (SVD):

$$\mathbf{F}_{M,i}^{\text{MAS}} = \mathbf{U}_{M,i}^{\text{MAS}} \boldsymbol{\Sigma}_{M,i}^{\text{MAS}} \mathbf{V}_{M,i}^{\text{MAS}^T} \quad (5)$$

where $\mathbf{U}_{M,i}^{\text{MAS}} \in \mathbb{R}^{85 \times p_i}$, $\boldsymbol{\Sigma}_{M,i}^{\text{MAS}} \in \mathbb{R}^{p_i \times p_i}$, and $\mathbf{V}_{M,i}^{\text{MAS}} \in \mathbb{R}^{25 \times p_i}$; p_i is the rank of $\mathbf{F}_{M,i}^{\text{MAS}}$. For recasting the solutions into matrix form, a general rule-of-thumb is to make the matrix as close to square as possible [42]. Equation (5) factorizes $\mathbf{F}_{M,i}^{\text{MAS}}$ in two orthonormal matrices, $\mathbf{U}_{M,i}^{\text{MAS}}$ and $\mathbf{V}_{M,i}^{\text{MAS}}$, which represent points on two distinct Grassmann manifolds:

$$\mathcal{G}_U \equiv \mathcal{G}(p, 85) = \{\text{span}(\mathbf{U}_M^{\text{MAS}}): \mathbf{U}_M^{\text{MAS}} \in \mathbb{R}^{85 \times p}\} \quad (6a)$$

$$\mathcal{G}_V \equiv \mathcal{G}(p, 25) = \{\text{span}(\mathbf{V}_M^{\text{MAS}}): \mathbf{V}_M^{\text{MAS}} \in \mathbb{R}^{25 \times p}\} \quad (6b)$$

where $p = \max(p_i)$, $i = 1, \dots, 300$. Matrix $\Sigma_{M,i}^{\text{MAS}} \in \mathbb{R}^{p \times p}$, is diagonal containing the most important eigenvalues. Next, diffusion maps are applied in order to unveil the structure of the Grassmann manifold. Note that unlike commonly employed diffusion maps on Euclidean space [7,43], a Grassmannian kernel [42] is employed in this case to define similarity between points on the Grassmann manifold. The overall kernel matrix $K(\mathbf{U}_M^{\text{MAS}}, \mathbf{V}_M^{\text{MAS}})$ is defined as

$$K(\mathbf{U}_M^{\text{MAS}}, \mathbf{V}_M^{\text{MAS}}) = K(\mathbf{U}_M^{\text{MAS}}) \circ K(\mathbf{V}_M^{\text{MAS}}) \quad (7)$$

where

$$K(\mathbf{U}_M^{\text{MAS}}): \mathcal{G}_U \times \mathcal{G}_U \rightarrow \mathbb{R}^{300 \times 300} \quad (8a)$$

$$K(\mathbf{V}_M^{\text{MAS}}): \mathcal{G}_V \times \mathcal{G}_V \rightarrow \mathbb{R}^{300 \times 300} \quad (8b)$$

are individual projection kernels defined on manifolds $\mathcal{G}(p, 85)$ and $\mathcal{G}(p, 25)$, respectively, and \circ denotes the Hadamard product. Finally, for each data point i , a set of diffusion coordinates $\boldsymbol{\theta}_{M,i}^{\text{MAS}} \in \mathbb{R}^q$ is obtained, q being the number of eigenvectors required to unveil the intrinsic structure of the Grassmann manifold. In this work, $q = 15$ was found to be sufficient to capture the essential features and geometric structure of both the MAS and CMPS fields.

3.3.2. Step II

In this step, two Gaussian processes are constructed:

$$\mathcal{GP}_{\boldsymbol{\theta}}^{\text{MAS}}: \mathbf{X}_M \rightarrow \boldsymbol{\theta}_M^{\text{MAS}} \quad (9a)$$

$$\mathcal{GP}_{\Sigma}^{\text{MAS}}: \mathbf{X}_M \rightarrow \Sigma_M^{\text{MAS}} \quad (9b)$$

where $\mathcal{GP}_{\boldsymbol{\theta}}^{\text{MAS}}$ and $\mathcal{GP}_{\Sigma}^{\text{MAS}}$ map the input random vector \mathbf{X}_M to the space of diffusion coordinates $\boldsymbol{\theta}_M^{\text{MAS}}$ and eigenvalues Σ_M^{MAS} , respectively. The mathematical formulation of these Gaussian processes is

$$\mathcal{GP}_{\boldsymbol{\theta}}^{\text{MAS}}(\mathbf{X}_M) = \mathcal{F}_{\boldsymbol{\theta}}(\mathbf{X}_M) + z_{\boldsymbol{\theta}}(\mathbf{X}_M, \omega) \quad (10a)$$

$$\mathcal{GP}_{\Sigma}^{\text{MAS}}(\mathbf{X}_M) = \mathcal{F}_{\Sigma}(\mathbf{X}_M) + z_{\Sigma}(\mathbf{X}_M, \omega) \quad (10b)$$

where $\mathcal{F}_{\boldsymbol{\theta}, \Sigma}(\mathbf{X}_M)$ represents the mean value (assumed to be constant in this study) and $z_{\boldsymbol{\theta}, \Sigma}(\mathbf{X}_M, \omega)$ represent zero-mean, stationary Gaussian processes, each defined in terms of a correlation function. Training of a Gaussian process involves calibrating the hyperparameters of this correlation function. In this work, a Gaussian correlation function is selected. Finally, for a new realization \mathbf{x}_M^* of the input parameter vector, each trained Gaussian process will return:

$$\mathcal{GP}_{\boldsymbol{\theta}}^{\text{MAS}}(\mathbf{x}_M^*) = \tilde{\boldsymbol{\theta}}_M^{\text{MAS}} \quad (11a)$$

$$\mathcal{GP}_{\Sigma}^{\text{MAS}}(\mathbf{x}_M^*) = \tilde{\Sigma}_M^{\text{MAS}} \quad (11b)$$

3.3.3. Step III

As discussed in the previous subsection, training of the Gaussian processes enables the prediction of the low-dimensional diffusion coordinates and eigenvalues, for any new realization of the input random vector. However, as the present study is interested in the behavior of the \mathbb{R}^{2125} - and \mathbb{R}^{6372} -valued MAS and CMPS

strain fields, the predicted reduced-order solutions must be mapped back to the original, very high dimensional space: the present study employs geometric harmonics [25] for this purpose.

Consider the diffusion coordinates, $\{\boldsymbol{\theta}_{M,i}^{\text{MAS}}\}_{i=1}^{300}$, of the strain field outputs corresponding to the training data. Two sets of data-points corresponding to these diffusion coordinates on the Grassmann manifolds $\mathcal{G}(p, 85)$ and $\mathcal{G}(p, 25)$ are $\{\mathbf{U}_{M,i}^{\text{MAS}}\}_{i=1}^{300}$ and $\{\mathbf{V}_{M,i}^{\text{MAS}}\}_{i=1}^{300}$, respectively. Using this data, two geometric harmonics models (for details, refer to Coifman and Lafon [25]) are constructed:

$$f_{\mathbf{U}}^{\text{MAS}}: \boldsymbol{\theta}_M^{\text{MAS}} \in \mathbb{R}^q \rightarrow \mathbf{U}_M^{\text{MAS}} \in \mathbb{R}^{85 \times p} \quad (12a)$$

$$f_{\mathbf{V}}^{\text{MAS}}: \boldsymbol{\theta}_M^{\text{MAS}} \in \mathbb{R}^q \rightarrow \mathbf{V}_M^{\text{MAS}} \in \mathbb{R}^{25 \times p} \quad (12b)$$

Here, $f_{\mathbf{U}}^{\text{MAS}}$ and $f_{\mathbf{V}}^{\text{MAS}}$ define mapping between diffusion coordinates and the corresponding matrices $\mathbf{U}_M^{\text{MAS}}$ and $\mathbf{V}_M^{\text{MAS}}$. A Gaussian or RBF kernel of unit length scale is selected for this purpose, with number of eigenpairs that are computed from the kernel set to 5. In a similar manner, the corresponding geometric harmonics models for the CMPS strain field output are also constructed.

The mappings defined in Eqs. (9) (i.e., Gaussian process surrogates) and (12) (i.e., geometric harmonics models) form the overall data-driven surrogate model, i.e., $\tilde{\mathcal{M}}^{\text{MAS}}: \mathbf{X}_M \rightarrow \mathbf{Y}_M^{\text{MAS}}$, which is used in this study to approximate the 2D subject-specific computational head model. For any given realization of the input random vector \mathbf{X}_M , the two Gaussian process surrogates in Eq. (9) predict the low-dimensional reduced outputs (i.e., diffusion coordinates of the low-dimensional latent space and the SVD diagonal matrix), while the two geometric harmonics models in Eq. (12) predict the two SVD orthogonal matrices. The three matrices \mathbf{U} , \mathbf{V} and $\boldsymbol{\Sigma}$ can then be combined as in Eq. (5) to yield the matrix version of the output, which is then recast as a column vector to yield the full, very high-dimensional vector strain output (corresponding to the random vector of MAS strain field, $\mathbf{Y}_M^{\text{MAS}}$). The corresponding data-driven surrogate model for predicting CMPS strain fields, i.e., $\tilde{\mathcal{M}}^{\text{CMPS}}: \mathbf{X}_M \rightarrow \mathbf{Y}_M^{\text{CMPS}}$, also works in a similar way.

All the calculation presented in this work are performed using two open-source Python packages: UQpy [44] for Grassmannian diffusion maps and Gaussian process, and *datafold* [45] for geometric harmonics.

3.4. Surrogate model validation

To assess the predictive ability of the data-driven surrogate models, leave-one-out cross-validation (LOO-CV) is conducted. In this method, 300 (i.e., full training dataset size) $\tilde{\mathcal{M}}^{\text{MAS}}$ and $\tilde{\mathcal{M}}^{\text{CMPS}}$ surrogate models are constructed, each trained using 299 input-output pairs from \mathcal{X}_M and $\mathbf{y}_M^{\text{MAS}}/\mathbf{y}_M^{\text{CMPS}}$, and applied to predict the output vector corresponding to the remaining realization of the input random vector (that is not used in the training process). The accuracy of the 300 models are evaluated using the scalar metric of coefficient of determination (R^2). The mean and standard deviation of this metric are reported. Mathematically, R^2 for a model tested on realization \mathbf{x}_M^* is given by

$$R^2 = 1 - \frac{\sum_j \left(\tilde{\mathcal{M}}_j(\mathbf{x}_M^*) - \mathcal{M}_j(\mathbf{x}_M^*) \right)^2}{\sum_j \left(\tilde{\mathcal{M}}_j(\mathbf{x}_M^*) - \bar{\mathcal{M}}(\mathbf{x}_M^*) \right)^2} \quad (13)$$

where $\mathcal{M}_j(\mathbf{x}_M^*)$ is the j^{th} component of the vector output (MAS or CMPS) obtained from the computational simulation of a 2D subject-specific head model with input material properties \mathbf{x}_M^* , and $\tilde{\mathcal{M}}_j(\mathbf{x}_M^*)$ is the corresponding vector output predicted by the data-driven surrogate model for the same set of material properties. $\tilde{\mathcal{M}}(\mathbf{x}_M^*)$ denotes the mean value of $\mathcal{M}_j(\mathbf{x}_M^*)$ over all j . Using Eq. (13), the accuracy of both the surrogate models, $\tilde{\mathcal{M}}^{\text{MAS}}$ (for MAS strain field output) and $\tilde{\mathcal{M}}^{\text{CMPS}}$ (for MAS strain field output) can be computed: for the former, j ranges from 1 to 2125 (i.e., number of white matter brain voxels in CC and CR), while for the latter, it ranges from 1 to 6372 (i.e., total number of brain voxels).

In addition to R^2 , which is used to measure the overall accuracy of the surrogate model, a second scalar metric of absolute relative error ϵ is employed to evaluate the local error at individual brain voxels (i.e., at a given j),

$$\epsilon_j = \left| \frac{\tilde{\mathcal{M}}_j(\mathbf{x}_M^*) - \mathcal{M}_j(\mathbf{x}_M^*)}{\mathcal{M}_j(\mathbf{x}_M^*)} \right| \quad (14)$$

3.5. Uncertainty propagation

Once the Gaussian process surrogates and geometric harmonics models are trained using the experimental design of 300 realizations and the resulting data-driven surrogate model is validated, the remaining 10000 realizations of the input random vector are utilized for uncertainty propagation (note, total 10300 realizations were obtained after the data-driven sampling in Section 3.2). This set of realizations is defined as $\mathcal{X}_{\text{M,UP}} = \{\mathbf{x}_M^{(301)}, \mathbf{x}_M^{(302)}, \dots, \mathbf{x}_M^{(10300)}\}$. Using the trained Gaussian process surrogates, $\mathcal{GP}_{\Theta}^{\text{MAS}}$ and $\mathcal{GP}_{\Sigma}^{\text{MAS}}$, the corresponding low-dimensional reduced outputs, $\{\tilde{\Theta}_{M,i}^{\text{MAS}}\}_{i=1}^{10000}$ (where $\tilde{\Theta}_{M,i}^{\text{MAS}} \in \mathbb{R}^q$) and $\{\tilde{\Sigma}_{M,i}^{\text{MAS}}\}_{i=1}^{10000}$ (where $\tilde{\Sigma}_{M,i}^{\text{MAS}} \in \mathbb{R}^{p \times p}$), are predicted. Next, using the trained geometric harmonics models, f_U^{MAS} and f_V^{MAS} , the set of matrices $\{\tilde{\mathbf{U}}_{M,i}^{\text{MAS}}\}_{i=1}^{10000}$ and $\{\tilde{\mathbf{V}}_{M,i}^{\text{MAS}}\}_{i=1}^{10000}$ are predicted. The matrix versions of the final MAS strain output, $\{\tilde{\mathbf{F}}_{M,i}^{\text{MAS}}\}_{i=1}^{10000}$, are then recovered using Eq. (5). Finally, the matrix solutions are recast to column vectors, i.e., $\{\tilde{\mathbf{F}}_{M,i}^{\text{MAS}} \in \mathbb{R}^{85 \times 25}\}_{i=1}^{10000} \rightarrow \{\tilde{\mathbf{y}}_{M,i}^{\text{MAS}} \in \mathbb{R}^{2125}\}_{i=1}^{10000}$, yielding the full, very high-dimensional solutions for all the 10000 realizations of the input random vector of visco-hyperelastic material properties. Different statistical measures of $\mathbf{Y}_M^{\text{MAS}}$ are computed from these 10000 output vectors. In a similar manner, UQ is conducted for the CMPS strain field via 10000 evaluations of the $\tilde{\mathcal{M}}^{\text{CMPS}}$ model (composed of $\mathcal{GP}_{\Theta}^{\text{CMPS}}$, $\mathcal{GP}_{\Sigma}^{\text{CMPS}}$, f_U^{CMPS} and f_V^{CMPS}).

4. Results

4.1. Model input realizations

As mentioned in the Section 3.2, a manifold learning-based data-driven method is employed in two steps in this study to generate realizations of the input random vector for the 2D subject-specific head model. In the first step, 900 realizations of the input random vectors corresponding to each of the four brain substructures (i.e., DG, CG, CC and CR) are individually generated. Figure 5(a) shows pair-wise correlation plots of the material properties in such realizations along with those in the available data for a representative

brain substructure, the corona radiata (CR). CR is one of the largest substructures in brain by volume, and equivalently, by the number of voxels. As there are four material properties associated with each substructure, six scatter plots (i.e., $C(4,2)$ combinations) are presented. Red data-points represent the 2534 available material properties' data points for this region after the removal of outliers (criteria: three scaled median absolute deviations), and blue data-points represent the generated 900 realizations. Normalized histograms of individual material parameters are also shown. From these plots, it is clear that the realizations follow the distribution of the original data, and thus it can be said that they are concentrated in subset $\mathcal{S}_4^{CR} \subset \mathbb{R}^4$ on which the probability distribution of the material properties of this substructure is concentrated. Similar agreement with the distribution of available data is seen for the other three brain substructures as well. With the realizations of all the four substructures, 300 realizations of the sixteen-dimensional input random vector of material properties for the entire head model are generated for training the data-driven surrogate model. Representation of all these input random vector components via pair-wise correlation plots would require 120 scatter plots (i.e., $C(16,2)$). For brevity, Figure 5(b) shows pair-wise correlation plots and normalized histograms of four material properties: one selected from each substructure. Again, it is seen that the new realizations (in blue) follow the distribution of the 900 realizations from individual brain substructures (in red) that were used as inputs for the data-driven generator of realizations in the second step. Thus, the generated realizations for the full head model are concentrated in the subset (initially unknown) $\mathcal{S}_{16} \subset \mathbb{R}^{16}$ on which the probability distribution of the sixteen input random vector components is concentrated.

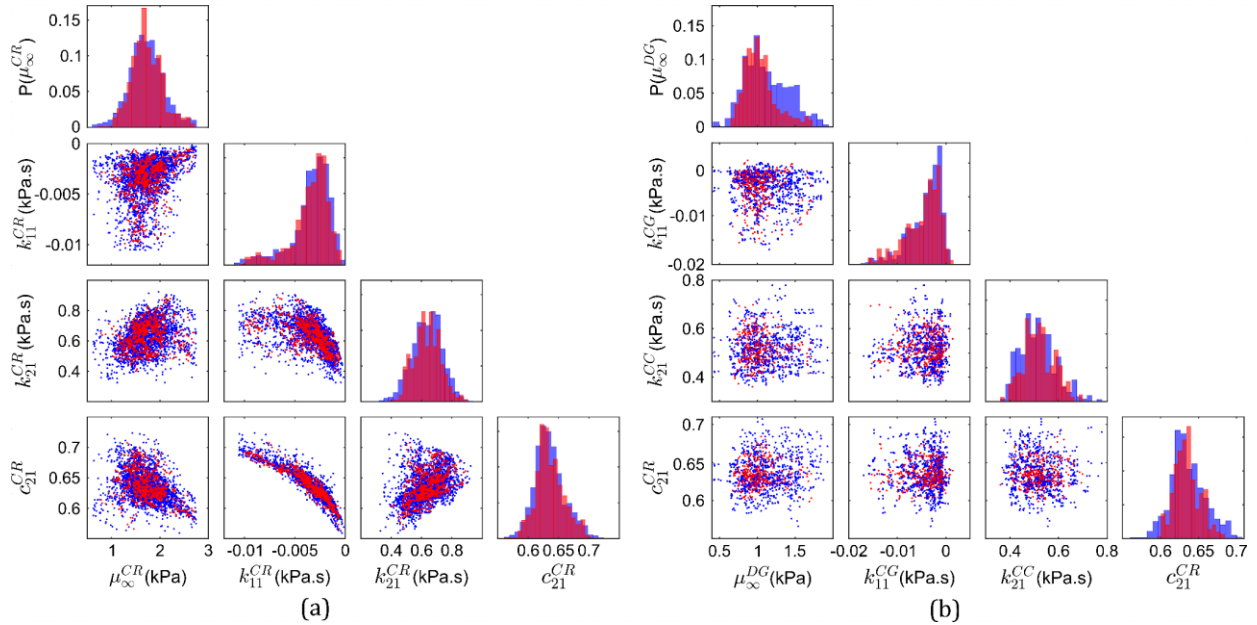


Figure 5. Pairwise correlation plots and normalized histograms of (a) four material properties of the corona radiata substructure: available data from MRE (in blue) and 900 generated realizations for this substructure (in red), and (b) four representative material properties from the four brain substructures: 900 realizations from individual substructures (in blue) and 300 new realizations of the overall 16D input random vector for the head model (in red).

4.2. Surrogate model

The 2D subject-specific head model simulations of the 300 input realizations provide the input-output (i.e., MAS or CMPS strain) pairs used as training-testing data for the data-driven surrogate models. Figure 6(a) compares the MAS strain field predicted by a representative surrogate model trained using 299 input-output pairs with the one obtained from head model simulation, for a particular set of material properties not part of the training input dataset. Note that these 2D fields are created by assigning each component of the strain vector output the spatial location (in the x-y plane) of a particular brain voxel; the correspondence between brain voxel location and strain vector components is a priori fixed. From this figure, a good agreement is observed between the computational model and the surrogate model for MAS strain. Figure 6(b) shows the spatial distribution of the absolute relative error metric ϵ (Eq. (14)), revealing a very high accuracy ($\epsilon \leq 0.1$) in regions of relatively high MAS, but a low accuracy ($\epsilon \geq 1$) in regions associated with negligible MAS. The latter is expected because in regions of negligible MAS, even a small discrepancy on the order of 0.001 mm/mm strain between the two models can lead to a very high absolute “relative” error. Overall, this representative surrogate model results in an excellent R^2 -value of 0.91 (calculated over all the MAS voxels). Figure 6(c) shows the corresponding comparison of CMPS strain fields resulted by the computational model and the representative surrogate model of CMPS strain, with the spatial distribution of ϵ shown in Fig. 6(d). Again, a good agreement is observed, this time, with a relatively uniform distribution of ϵ . For this representative surrogate model, an R^2 -value of 0.88 is obtained over all the brain voxels.

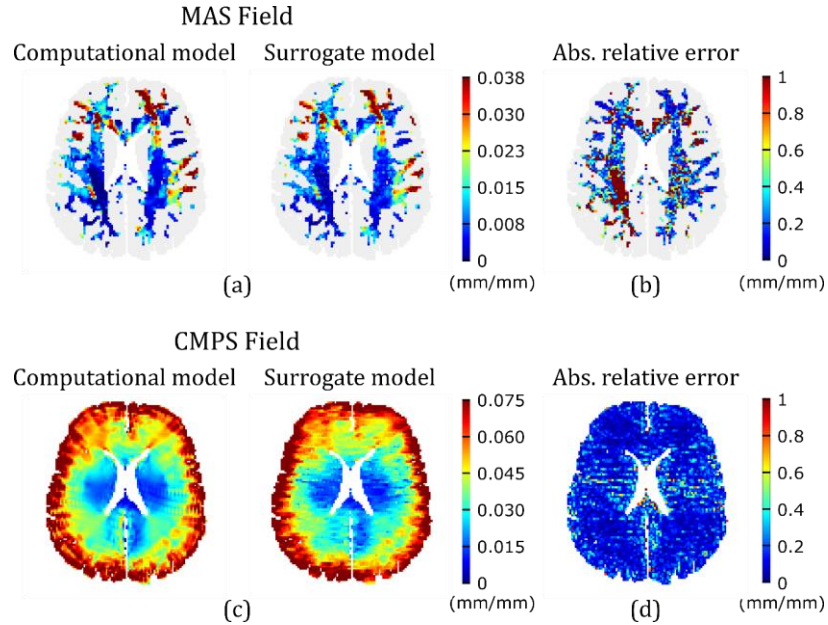


Figure 6. Comparison of prediction strain fields for a representative realization of the input random vector (i.e., $\mathbf{x}_M^0 = (0.744, -0.158, 0.467, 0.908, 0.915, -0.450\text{E-}2, 0.239, 0.716, 2.05, -0.141\text{E-}2, 0.643, 0.618, 1.66, -0.181\text{E-}2, 0.513, 0.619)$; see order of material properties in Eq. (3), and units in Table 1) by surrogate models trained using the remaining 299 input-output pairs, with the corresponding fields resulted by the computational head model: (a) MAS strain field, (c) CMPS strain field. The corresponding absolute relative errors for the MAS and CMPS strain fields are shown in (b) and (d), respectively.

Overall, for the two data-driven surrogate models developed in this work for MAS and CMPS strain fields, LOO-CV results in an R^2 of 0.84 ± 0.08 for the MAS case, and 0.81 ± 0.10 for the CMPS case. In addition to reasonably approximating the computational head model with a small training dataset, the surrogate

models also lead to a significant reduction in computational cost. For the representative models in Fig. 6, the two surrogate model runs for predicting MAS and CMPS strain fields completed in 0.008 ± 0001 seconds (p -value < 0.05 , based on 5 runs) on a personal computer, while the corresponding MPM simulation of the computational model completed in 9948.64 seconds on a supercomputing cluster (with 72 parallel tasks). This means that the surrogate model offers more than a million times faster performance!

4.3. Uncertainty in the strain-response of the 2D subject-specific model

The trained surrogate models are used to predict strain outputs corresponding to the 10000 additional input realizations (see Section 3.5) for uncertainty quantification of the computational head model. Figure 7(a) plots the p^{th} -percentile MAS (denoted by MAS_p) for the 2D subject-specific head model investigated in this work in the $p \in [5, 100]$ range: data-points represent the average values, while error bars represent one standard deviation. The corresponding p^{th} -percentile CMPS (denoted by $CMPS_p$) are shown in Fig. 7(b). From these figures, the absolute values of standard deviations for both MAS_p and $CMPS_p$ increase with the percentile score. For a better insight into the relative uncertainty of strain outputs, Fig. 7(c) plots the coefficient of variation (CV), defined as the ratio of the mean to the standard deviation, for the two strain outputs as a function of the percentile score. For MAS_p values evaluated at less than 20-percentile, CV is greater than $1/3$, i.e., the mean is less than three times the standard deviation. This is equivalent to a signal-to-noise ratio [46] (SNR) (i.e., the reciprocal of CV) of greater than 3. Thus, for low percentiles, the MAS_p strain output is associated with a high uncertainty. Interestingly, for 5-percentile MAS, $CV = 4.55$, which means the noise is more than four times the signal! With increasing percentile score, the CV of MAS_p decreases or stays nearly constant up to $p = 95$, and then increases again to ~ 0.41 for the peak MAS evaluated at 100th percentile. Unlike MAS_p , for $CMPS_p$, the CV at all the investigated percentile scores except $p = 100$ (i.e., peak CMPS) are considerably less than $1/3$, suggesting a consistently low uncertainty. For both MAS_p and $CMPS_p$, a low CV is observed in the 50- to 95-percentile score range. As 50- and 95-percentile MAS and CMPS are commonly employed in the brain biomechanics community for the prediction and vulnerability assessment to brain injury [6,30,47], the uncertainty in these brain injury metrics for subject-specific models is reasonably low (actual values of mean, standard deviation and CV are listed in Table 2). Due to their insignificant effect on brain injury prediction, strains evaluated at percentile scores below 50 hold lesser importance.

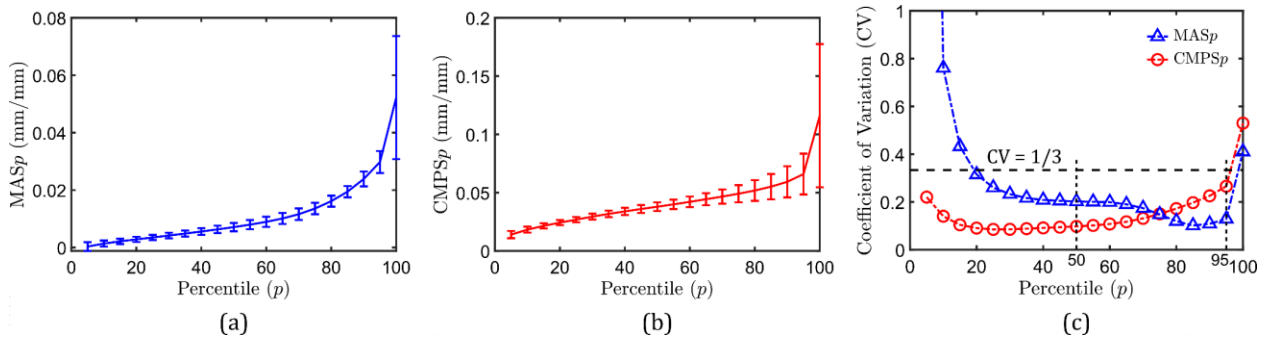


Figure 7. Uncertainty in the p^{th} percentile MAS (MAS_p) and p^{th} percentile CMPS ($CMPS_p$) outputs of the 2D head model: (a) MAS_p versus p , (b) $CMPS_p$ versus p , and (c) CV of MAS_p and $CMPS_p$ versus p .

To visualize uncertainty in the full-field strain outputs, Figs. 8(a) and 8(b) plot CV at all the voxels in the MAS and CMPS strain fields, respectively, that are associated with average strain greater than the average

50-percentile value. It is seen that the uncertainty in MAS is relatively high ($CV > 0.4$) in the right-frontal region of corona radiata (note, right side of brain is on the left in the figure), and is reasonably low in the corpus callosum and the corona radiata in left brain-hemisphere. In the case of the CMPS field, a low uncertainty is observed in the majority of the brain layer area, with relatively high CV only in the left and right peripheries of the cerebrum gray matter near its interface with the SAS. Overall, the average CV of MAS and CMPS fields in the two figures is 0.29 and 0.20, respectively.

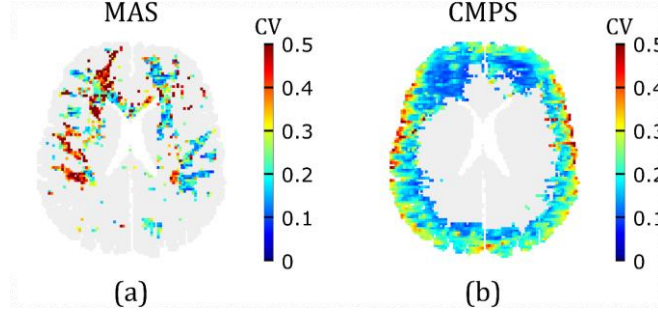


Figure 8. Uncertainty in the strain field outputs of the 2D head model: (a) CV in the MAS in brain voxels where MAS is greater than the average 50-percentile MAS (i.e., $\overline{MAS50}$); (b) CV in the CMPS in brain voxels where CMPS is greater than the average 50-percentile CMPS (i.e., $\overline{CMPS50}$).

Table 2. Mean and standard deviation of the scalar strain outputs of the 2D subject-specific head model, which are commonly employed as brain injury predictor variables.

Scalar MAS output	Mean	Std. dev.	CV	Scalar CMPS output	Mean	Std. dev.	CV
MAS50 (mm/mm)	0.0071	0.0014	0.20	CMPS50 (mm/mm)	0.0379	0.0037	0.10
MAS95 (mm/mm)	0.0298	0.0038	0.13	CMPS95 (mm/mm)	0.0659	0.0175	0.27
AF- $\overline{MAS50}$	0.1650	0.0259	0.16	AF- $\overline{CMPS50}$	0.4851	0.0888	0.18
AF- $\overline{MAS95}$	0.0159	0.0083	0.52	AF- $\overline{CMPS95}$	0.0586	0.0776	1.32

Further, the uncertainty in the area fraction of brain that is associated with strain greater than a certain threshold is analyzed. In this regard, $AF-\overline{MASp}$ denotes the area fraction with MAS greater than the mean p^{th} -percentile MAS threshold (i.e., \overline{MASp}), and $AF-\overline{CMPSp}$ denotes the area fraction with CMPS greater than the mean p^{th} -percentile CMPS threshold (i.e., \overline{CMPSp}). Figures 9(a) and 9(b) plot $AF-\overline{MASp}$ and $AF-\overline{CMPSp}$ versus p , respectively. As expected, smaller (average) area fractions of the brain layer are associated with larger strain values that are evaluated at higher percentiles, leading to monotonically decreasing responses. In the case of $AF-\overline{MASp}$, the absolute value of the standard deviation generally decreases with the percentile score. The CV (see Fig. 9(c)), on the other hand, increases with the percentile score especially in the low and high percentile regimes; nevertheless, it consistently stays considerably below 1/3 for all p except at $p = 100$, when $CV = 0.52$. Unlike $AF-\overline{MASp}$, $AF-\overline{CMPSp}$ is associated with a much higher uncertainty at high percentile thresholds of $p > 60$. Overall, compared to the uncertainty in the p^{th} -percentile strain outputs shown in Fig. 7, the uncertainty in the area fraction-based outputs shown here is much higher. It is important to note that in the case of 3D head injury models, the volume fractions of brain with MAS and CMPS above certain strain thresholds are commonly used as injury predictor variables[6]. As the present head model is used to simulate non-injurious loading, the available injury thresholds in the literature are generally much higher than the average strain values in this study [5,33,47]. Further, the exact values of available thresholds vary widely, and no consensus has been reached on what threshold value to use [6,29]. Thus, in this study, 50- and 95-percentile MAS and CMPS are considered as strain thresholds

to analyze the relative vulnerability to brain injury. The associated statistical metrics of $\overline{\text{AF-MAS50}}$, $\overline{\text{AF-MAS95}}$, $\overline{\text{AF-CMPS50}}$, and $\overline{\text{AF-CMPS95}}$ are reported in Table 2. Clearly, a high uncertainty exists in these area/volume fraction-based injury metrics for the subject-specific 2D head model.

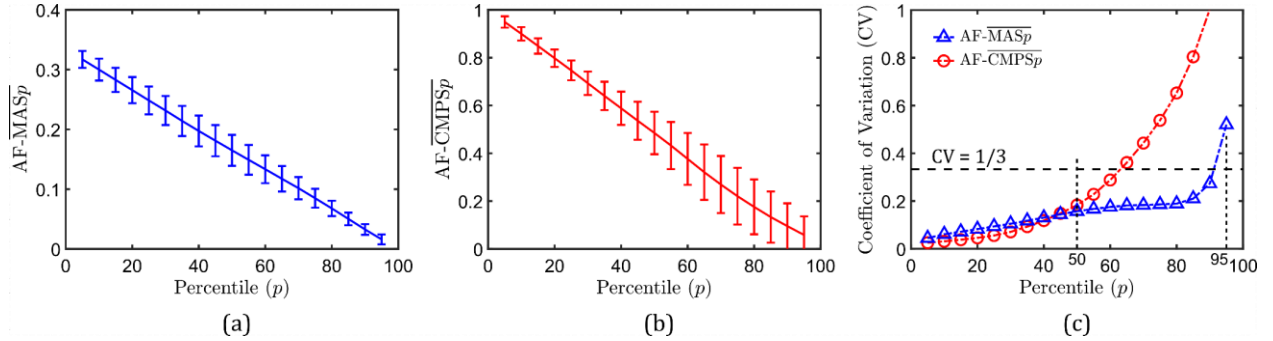


Figure 9. Uncertainty in the predicted area fractions ($\overline{\text{AF-MAS}p}$ and $\overline{\text{AF-CMPS}p}$) associated with MAS and CMPS values greater than their mean p^{th} percentile thresholds: (a) $\overline{\text{AF-MAS}p}$ versus p , (b) $\overline{\text{AF-CMPS}p}$ versus p , and (c) CV of $\overline{\text{AF-MAS}p}$ and $\overline{\text{AF-CMPS}p}$ versus p .

Finally, the spatial uncertainty in the prediction of highly strained regions based on the MAS and CMPS-based injury predictor variables is studied. In this regard, four probability values are computed for every brain voxel as

$$P_j^{\text{MAS} > \overline{\text{MAS50}}} = \frac{\text{card}\{\tilde{\mathbf{y}}_{M,i}^{\text{MAS}}(j) > \overline{\text{MAS50}}\}}{10000}, \quad P_j^{\text{MAS} > \overline{\text{MAS95}}} = \frac{\text{card}\{\tilde{\mathbf{y}}_{M,i}^{\text{MAS}}(j) > \overline{\text{MAS95}}\}}{10000} \quad (16a)$$

$$P_j^{\text{CMPS} > \overline{\text{CMPS50}}} = \frac{\text{card}\{\tilde{\mathbf{y}}_{M,i}^{\text{CMPS}}(j) > \overline{\text{CMPS50}}\}}{10000}, \quad P_j^{\text{CMPS} > \overline{\text{CMPS95}}} = \frac{\text{card}\{\tilde{\mathbf{y}}_{M,i}^{\text{CMPS}}(j) > \overline{\text{CMPS95}}\}}{10000} \quad (16b)$$

where $P_j^{\text{MAS} > \overline{\text{MAS}p}}$ ($p = 50, 95$) denotes the probability that the MAS value predicted at j^{th} brain voxel (i.e., $\tilde{\mathbf{y}}_{M,i}^{\text{MAS}}(j)$) for the i^{th} evaluated realization of the head model (i ranges from 1 to 10000) is greater than $\overline{\text{MAS}p}$. $\text{card}\{\cdot\}$ operator denotes the cardinality (i.e., number of components) of a set. Similarly, $P_j^{\text{CMPS} > \overline{\text{CMPS}p}}$ denotes the corresponding probability that CMPS at j^{th} brain voxel (i.e., $\tilde{\mathbf{y}}_{M,i}^{\text{CMPS}}(j)$) for i^{th} realization is greater than $\overline{\text{CMPS}p}$.

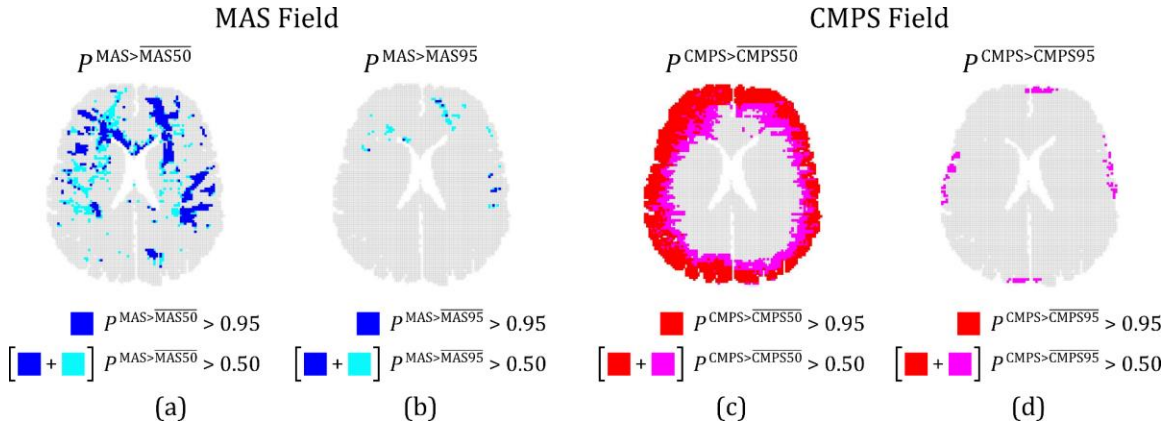


Figure 10. (a) Predicted regions where the probability of MAS being greater than $\overline{\text{MAS50}}$ (i.e., $P^{\text{MAS} > \overline{\text{MAS50}}}$), is at least 0.95 (blue) or 0.5 (cyan and blue). Corresponding regions for (b) $P^{\text{MAS} > \overline{\text{MAS95}}}$, (c) $P^{\text{CMPS} > \overline{\text{CMPS50}}}$, and (d) $P^{\text{CMPS} > \overline{\text{CMPS95}}}$. In (c) and (d), regions where the relevant probability measure is at least 0.95 is shown in red, and where it is at least 0.5 is represented by the combined red and magenta regions.

Figure 10(a) shows the predicted area in the brain layer where $P^{\text{MAS} > \overline{\text{MAS50}}}$ is at least 0.5 (combined blue and cyan regions), which corresponds to a 50% chance that MAS (at a given brain voxel) is greater than $\overline{\text{MAS50}}$. Comparing this to the considerably smaller region (in blue) with a 95% chance (i.e., $P^{\text{MAS} > \overline{\text{MAS50}}} \geq 0.95$), a significant uncertainty exists in the predicted area of brain with MAS greater than $\overline{\text{MAS50}}$. Similar conclusions can be drawn for the predicted area where MAS is greater than $\overline{\text{MAS95}}$ (see Fig. 10(b)), and for the predicted areas where CMPS is greater than $\overline{\text{CMPS50}}$ and $\overline{\text{CMPS95}}$, respectively (Figs. 10(c-d)). Interestingly, from Fig. 10(d), there is no brain voxel where at least 95% of the realizations result in a CMPS that is greater than $\overline{\text{CMPS95}}$, even though a 2% 2D brain area exists where at least 50% of the realizations result in a CMPS that is greater than $\overline{\text{CMPS95}}$. For the same strain measure, 24% brain area corresponds to $P^{\text{CMPS} > \overline{\text{CMPS95}}} \geq 0.05$. This striking difference between the predicted regions with CMPS greater than $\overline{\text{CMPS95}}$ likely resulted in the very high uncertainty ($\text{CV} > 1$) of the AF-CMPS95 injury predictor variable (Table 2).

5. Discussion

The present study proposed a manifold learning-based data-driven framework for UQ of computational head models. This framework is composed of two stages: in the first stage, a data-driven generator of realizations is used to allow non-parametric estimation of probability distribution and sampling of the input random vector directly from the available data; in the second stage, a data-driven surrogate model is constructed, which employs manifold learning for dimensionality reduction of the high-dimensional output, and Gaussian process surrogates and geometric harmonics models to create end-to-end mappings between high-dimensional input and output. This general framework allows UQ in high-fidelity computational head models that are associated with high computational cost and high-dimensional inputs and output strain fields. A few examples of input parameters that can be analyzed using the proposed surrogate modeling approach are head geometry (variables: length, breadth, height, circumference, aspect ratio, volume, etc.), material properties (e.g., variability across population), and boundary conditions (variables: peak acceleration, loading duration, etc.).

As a sample problem, a 2D version of a recently developed 3D subject-specific head model by the authors is selected. The choice of the axial 2D brain slice is dictated by the maximum brain layer area fraction with MAS greater than the 50- and 95-percentile MAS thresholds (over the entire 3D brain volume). Subject-specific head models derive all three model inputs from the same living human subject. It is shown in this work that even in these types of models that are commonly assumed to be associated with low-uncertainty[14], inter-region variability of full-field material properties can still be a significant source for variability in the simulated strain fields. Overall, the 2D subject-specific head model considered in this work is associated with high computational cost, a 16-dimensional input of nonlinear visco-hyperelastic material properties of different brain regions, and 2125- and 6372-dimensional MAS and CMPS strain field outputs.

Using the data-driven generator of realizations, 10300 total realizations of the 16D input random vector are generated directly from the available MRE data, out of which 300 realizations are used as training data for the surrogate model. It is seen that these realizations are consistent with the distribution of the available data, which highlights the ability of this method of accurately discovering the a priori unknown probability distribution of the input parameter data as well as the unknown subset on which it was concentrated. Note that the space-filling property of this data-driven method is proportional to the number of generated realizations. For example, normalized histograms (as in Fig. 5) of the available data with 50 generated realizations (instead of 300) are shown in the supplementary material, revealing a greater mismatch between the two distributions when small number of training samples are generated.

Using the 300 pairs of inputs and outputs generated using the computational model simulations, the data-driven surrogate model is trained. It is shown that the trained surrogate model results in a good approximation of the very high-dimensional output of the computational model, with LOO-CV resulting in an R^2 of 0.84 ± 0.08 for the MAS field, and 0.81 ± 0.10 for the CMPS field. The overall accuracy of a surrogate model (i.e., R^2) generally improves with the training dataset size, eventually reaching an asymptote for a sufficiently large training dataset [48]. The R^2 versus training dataset size plot for surrogate model in this study is shown in the supplementary material. Even at a training dataset of only 25 input-output pairs, mean R^2 values of greater than 0.70 were obtained for both surrogate models, which increased to asymptotic values at an approximate data size of 100 pairs. Note, however, that input parameters from such small training dataset will likely be in a relatively poor agreement with the distribution of the original data. Further, in this study, an excellent improvement is obtained in the computational cost, with the surrogate model simulations running more than a million times faster compared to the corresponding computational model simulations.

Forward uncertainty propagation using the trained surrogate model shows that CV of MAS_p (i.e., MAS evaluated at p^{th} percentile) is greater than 1/3 at lower percentile scores of less than 20, suggesting high uncertainty for smaller values of this strain measure. A high uncertainty is also noted for peak strain values of both MAS and CMPS (i.e., at $p = 100$). In the range of 50- to 95-percentile scores, the uncertainty in strains is reasonably low, as the CV is consistently lower than 0.27. In addition to the scalar strain percentile outputs, the uncertainty in the full-field strain output is also analyzed. A considerable variation in CV is seen across the brain layer for both the investigated strain measures, pointing to regions of relatively low or high uncertainty. Specifically, for MAS, relatively high CV is observed in the right-frontal region of corona radiata that is associated with small strain magnitudes. On the contrary, for CMPS, relatively high CV is observed in the left and right periphery of brain that are associated with large strain magnitudes. Interestingly, these peripheral regions are also associated with artifacts in MRE measurements[49]. The spatial variation of model uncertainty further highlights the importance of considering full, high-dimensional strain outputs in UQ of head models. In-depth studies on such spatial varying uncertainties can guide specific modifications in the model and improvements in the experiments that provide input data.

In addition to the 50- and 95-percentile MAS and CMPS, brain area fraction-based injury predictor variables are analyzed in this study. Compared to the percentile strain-based variables, the area fraction-based variables are associated with a higher uncertainty. Notably, $AF-\overline{CMPS_p}$ is associated with a very high uncertainty at larger strain thresholds (observed at $p > 60$). Further, the uncertainty in the predicted regions where strain is greater than 50- and 95-percentile strain thresholds is studied. For MAS, while at least 95% of the realizations (out of 10000) predicted $AF-\overline{MAS50}$ of greater than 0.09, the corresponding $AF-\overline{MAS50}$

predicted by at least 50% is much greater at 0.16. In terms of probability, there is ~77.77% larger region where probability of MAS being greater than $\overline{\text{MAS50}}$ is at least 0.5, compared to the corresponding region with 0.95 probability. Similarly, significant differences in predicted regions with strain above threshold values are also seen in the case of CMPS. Overall, differences in the uncertainty between different injury predictor variables can guide selection of appropriate injury predictors for assessing the injury risk, which will be a subject of future research.

6. Conclusion

A generalized framework is proposed for UQ of computational head models, which is demonstrated by application on a 2D subject-specific head model. In this model, the head geometry is derived from biomedical imaging, while nonlinear visco-hyperelastic material properties across the brain are obtained using in-vivo MRE. The model is used to simulate a non-injurious rotational acceleration to the head about the I/S axis. It is shown that inter-region variability of material properties is a significant source of uncertainty in these models. A data-driven method is used to sample multiple realizations of the input random vector, which provide training dataset for the development of two manifold learning-based surrogate models to provide a low-cost mapping between input and the MAS and CMPS strain field outputs, respectively. The surrogate models are composed of Gaussian processes, which create a mapping between input and reduced order outputs, and geometric harmonics models, which allow out-of-sample predictions of full, high-dimensional outputs from new realizations. It is shown that surrogate models trained using 300 input-output pairs predict the strain fields with good accuracy while offering excellent computational cost reduction. Uncertainty propagation via this surrogate model leads to UQ estimates of full-field strain as well as of certain scalar strain variables that are commonly employed as predictor variables for estimation of brain injury risk. Results reveal that among the strain percentile-based and area fraction-based injury predictor variables, the latter are associated with a higher uncertainty. A spatial variation of uncertainty in the strain field is also observed.

Acknowledgements

This research was supported by the National Institute of Health under Grant No. U01 NS11212.

References

- [1] National Center for Health Statistics: Mortality Data on CDC WONDER, (n.d.). <https://wonder.cdc.gov/mcd.html>.
- [2] D. Pavlovic, S. Pekic, M. Stojanovic, V. Popovic, Traumatic brain injury: neuropathological, neurocognitive and neurobehavioral sequelae, *Pituitary*. 22 (2019) 270–282. <https://doi.org/10.1007/s11102-019-00957-9>.
- [3] N.A. Shaw, The neurophysiology of concussion, *Prog. Neurobiol.* 67 (2002) 281–344. [https://doi.org/10.1016/S0301-0082\(02\)00018-7](https://doi.org/10.1016/S0301-0082(02)00018-7).
- [4] D. Sahoo, C. Deck, R. Willinger, Brain injury tolerance limit based on computation of axonal strain, *Accid. Anal. Prev.* 92 (2016) 53–70. <https://doi.org/10.1016/j.aap.2016.03.013>.
- [5] E.G. Takhounts, M.J. Craig, K. Moorhouse, J. McFadden, V. Hasija, Development of Brain Injury Criteria (BrIC), in: *Stapp Car Crash J.*, 2013: pp. 243–266. <https://doi.org/10.4271/2013-22-0010>.

- [6] W. Zhao, Y. Cai, Z. Li, S. Ji, Injury prediction and vulnerability assessment using strain and susceptibility measures of the deep white matter, *Biomech. Model. Mechanobiol.* 16 (2017) 1709–1727. <https://doi.org/10.1007/s10237-017-0915-5>.
- [7] R.G. Steen, R.M. Hamer, J.A. Lieberman, Measuring Brain Volume by MR Imaging: Impact of Measurement Precision and Natural Variation on Sample Size Requirements, *Am. J. Neuroradiol.* 28 (2007) 1119–1125. <https://doi.org/10.3174/ajnr.A0537>.
- [8] B. Rashid, M. Destrade, M.D. Gilchrist, Mechanical characterization of brain tissue in tension at dynamic strain rates, *J. Mech. Behav. Biomed. Mater.* 33 (2014) 43–54. <https://doi.org/10.1016/j.jmbbm.2012.07.015>.
- [9] A. TAMURA, S. HAYASHI, K. NAGAYAMA, T. MATSUMOTO, Mechanical Characterization of Brain Tissue in High-Rate Extension, *J. Biomech. Sci. Eng.* 3 (2008) 263–274. <https://doi.org/10.1299/jbse.3.263>.
- [10] M.T. Prange, S.S. Margulies, Regional, Directional, and Age-Dependent Properties of the Brain Undergoing Large Deformation, *J. Biomech. Eng.* 124 (2002) 244. <https://doi.org/10.1115/1.1449907>.
- [11] W. Zhao, B. Choate, S. Ji, Material properties of the brain in injury-relevant conditions – Experiments and computational modeling, *J. Mech. Behav. Biomed. Mater.* 80 (2018) 222–234. <https://doi.org/10.1016/j.jmbbm.2018.02.005>.
- [12] K. Teferra, X.G. Tan, A. Iliopoulos, J. Michopoulos, S. Qidwai, Effect of human head morphological variability on the mechanical response of blast overpressure loading, *Int. j. Numer. Method. Biomed. Eng.* 34 (2018) e3109. <https://doi.org/10.1002/cnm.3109>.
- [13] D. Sahoo, C. Deck, R. Willinger, Development and validation of an advanced anisotropic visco-hyperelastic human brain FE model, *J. Mech. Behav. Biomed. Mater.* 33 (2014) 24–42. <https://doi.org/10.1016/j.jmbbm.2013.08.022>.
- [14] S. Ganpule, N.P. Daphalapurkar, K.T. Ramesh, A.K. Knutsen, D.L. Pham, P. V. Bayly, J.L. Prince, A Three-Dimensional Computational Human Head Model That Captures Live Human Brain Dynamics, *J. Neurotrauma.* 34 (2017) 2154–2166. <https://doi.org/10.1089/neu.2016.4744>.
- [15] S. Ji, W. Zhao, J.C. Ford, J.G. Beckwith, R.P. Bolander, R.M. Greenwald, L.A. Flashman, K.D. Paulsen, T.W. McAllister, Group-Wise Evaluation and Comparison of White Matter Fiber Strain and Maximum Principal Strain in Sports-Related Concussion, *J. Neurotrauma.* 32 (2015) 441–454. <https://doi.org/10.1089/neu.2013.3268>.
- [16] B. Sudret, S. Marelli, J. Wiart, Surrogate Models for Uncertainty Quantification : An Overview, in: 2017 11th Eur. Conf. Antennas Propag., IEEE, Paris, 2017: pp. 793–797. <https://doi.org/10.23919/EuCAP.2017.7928679>.
- [17] D.G. Giovanis, M.D. Shields, Uncertainty quantification for complex systems with very high dimensional response using Grassmann manifold variations, *J. Comput. Phys.* 364 (2018) 393–415. <https://doi.org/10.1016/j.jcp.2018.03.009>.
- [18] A.P. Iliopoulos, J.G. Michopoulos, P. Avery, C. Farhat, K. Teferra, S. Qidwai, Towards Model Order Reduction for Uncertainty Propagation in Blast-Induced Traumatic Brain Injury, in: Vol. 1 37th Comput. Inf. Eng. Conf., American Society of Mechanical Engineers, 2017: pp. 1–12. <https://doi.org/10.1115/DETC2017-67556>.
- [19] T. Aymard, T. Fogang, Finite Element Simulation of Human Head under Frontal Impact with Uncertainties in Constitutive Modeling and Material Parameters, The University at Buffalo, State

- University of New York, 2015. <https://www.proquest.com/docview/1733327644?pq-origsite=gscholar&fromopenview=true>.
- [20] S. Kacker, The Role of Constitutive Model in Traumatic Brain Injury Prediction, University of Cincinnati, 2019. https://etd.ohiolink.edu/apexprod/rws_etd/send_file/send?accession=ucin1563874757653453&disposition=inline.
 - [21] M. Hazay, D. Dénes, I. Bojtár, The probability of traumatic brain injuries based on tissue-level reliability analysis., *Acta Bioeng. Biomech.* 21 (2019) 141–152. <https://doi.org/10.5277/ABB-01281-2018-02>.
 - [22] C. Soize, R. Ghanem, Data-driven probability concentration and sampling on manifold, *J. Comput. Phys.* 321 (2016) 242–258. <https://doi.org/10.1016/j.jcp.2016.05.044>.
 - [23] K.R.M. dos Santos, D.G. Giovanis, M.D. Shields, Grassmannian diffusion maps based dimension reduction and classification for high-dimensional data, *ArXiv*. (2020) 1–26. <http://arxiv.org/abs/2009.07547>.
 - [24] C.K.I. Williams, C.E. Rasmussen, Gaussian processes for regression, in: D.S. Touretzky, M.C. Mozer, M.E. Hasselmo (Eds.), *Adv. Neural Inf. Process. Syst.* 8, MIT, 1996.
 - [25] R.R. Coifman, S. Lafon, Geometric harmonics: A novel tool for multiscale out-of-sample extension of empirical functions, *Appl. Comput. Harmon. Anal.* 21 (2006) 31–52. <https://doi.org/10.1016/j.acha.2005.07.005>.
 - [26] K. Upadhyay, A. Alshareef, A.K. Knutsen, C.L. Johnson, A. Carass, P. V. Bayly, K.T. Ramesh, Development and Validation of Subject-Specific 3D Human Head Models Based on a Nonlinear Visco-Hyperelastic Constitutive Framework, *BioRxiv*. (2021) 1–27.
 - [27] L. V. Hiscox, C.L. Johnson, E. Barnhill, M.D.J. McGarry, J. Huston, E.J.R. van Beek, J.M. Starr, N. Roberts, Magnetic resonance elastography (MRE) of the human brain: technique, findings and clinical applications, *Phys. Med. Biol.* 61 (2016) R401–R437. <https://doi.org/10.1088/0031-9155/61/24/R401>.
 - [28] L. V. Hiscox, C.L. Johnson, M.D.J. McGarry, M. Perrins, A. Littlejohn, E.J.R. van Beek, N. Roberts, J.M. Starr, High-resolution magnetic resonance elastography reveals differences in subcortical gray matter viscoelasticity between young and healthy older adults, *Neurobiol. Aging*. 65 (2018) 158–167. <https://doi.org/10.1016/j.neurobiolaging.2018.01.010>.
 - [29] A.K. Knutsen, A.D. Gomez, M. Gangolli, W. Wang, D. Chan, Y. Lu, E. Christoforou, J.L. Prince, P. V. Bayly, J.A. Butman, D.L. Pham, In vivo estimates of axonal stretch and 3D brain deformation during mild head impact, *Brain Multiphysics*. (2020) 100015. <https://doi.org/10.1016/j.brain.2020.100015>.
 - [30] R.W. Carlsen, A.L. Fawzi, Y. Wan, H. Kesari, C. Franck, A quantitative relationship between rotational head kinematics and brain tissue strain from a 2-D parametric finite element analysis, *Brain Multiphysics*. 2 (2021) 100024. <https://doi.org/10.1016/j.brain.2021.100024>.
 - [31] R.M. Wright, A. Post, B. Hoshizaki, K.T. Ramesh, A Multiscale Computational Approach to Estimating Axonal Damage under Inertial Loading of the Head, *J. Neurotrauma*. 30 (2013) 102–118. <https://doi.org/10.1089/neu.2012.2418>.
 - [32] S. Wakana, L.M. Nagae-Poetscher, H. Jiang, P. van Zijl, X. Golay, S. Mori, Macroscopic orientation component analysis of brain white matter and thalamus based on diffusion tensor imaging, *Magn. Reson. Med.* 53 (2005) 649–657. <https://doi.org/10.1002/mrm.20386>.

- [33] C. Giordano, S. Kleiven, Evaluation of axonal strain as a predictor for mild traumatic brain injuries using finite element modeling, *Stapp Car Crash J.* 58 (2014) 29–61. <https://www.sae.org/content/2014-22-0002/>.
- [34] K. Upadhyay, G. Subhash, D. Spearot, Visco-hyperelastic constitutive modeling of strain rate sensitive soft materials, *J. Mech. Phys. Solids.* 135 (2020) 103777. <https://doi.org/10.1016/j.jmps.2019.103777>.
- [35] J.R. MACDONALD, Some Simple Isothermal Equations of State, *Rev. Mod. Phys.* 38 (1966) 669–679. <https://doi.org/10.1103/RevModPhys.38.669>.
- [36] H. Mao, L. Zhang, B. Jiang, V. V. Genthikatti, X. Jin, F. Zhu, R. Makwana, A. Gill, G. Jandir, A. Singh, K.H. Yang, Development of a Finite Element Human Head Model Partially Validated With Thirty Five Experimental Cases, *J. Biomech. Eng.* 135 (2013). <https://doi.org/10.1115/1.4025101>.
- [37] J.E. Galford, J.H. McElhaney, A viscoelastic study of scalp, brain, and dura, *J. Biomech.* 3 (1970) 211–221. [https://doi.org/10.1016/0021-9290\(70\)90007-2](https://doi.org/10.1016/0021-9290(70)90007-2).
- [38] J.H. McElhaney, J.W. Melvin, V.L. Roberts, H.D. Portnoy, Dynamic Characteristics of the Tissues of the Head, in: R.M. Kenedi (Ed.), *Perspect. Biomed. Eng.*, Palgrave Macmillan UK, London, 1973: pp. 215–222. https://doi.org/10.1007/978-1-349-01604-4_34.
- [39] W. Goldsmith, Biomechanics of head injury, in: Y. Fung (Ed.), *Biomech. Its Found. Object.*, Prentice Hall, Englewood Cliffs, NJ, 1972: pp. 585–634.
- [40] K. Kontolati, D. Loukrezis, K.R.M. dos Santos, D.G. Giovanis, M.D. Shields, Manifold learning-based polynomial chaos expansions for high-dimensional surrogate models, (2021) 1–29. <http://arxiv.org/abs/2107.09814>.
- [41] T. O’Leary-Roseberry, U. Villa, P. Chen, O. Ghattas, Derivative-informed projected neural networks for high-dimensional parametric maps governed by PDEs, *Comput. Methods Appl. Mech. Eng.* 388 (2022) 114199. <https://doi.org/10.1016/j.cma.2021.114199>.
- [42] D.G. Giovanis, M.D. Shields, Data-driven surrogates for high dimensional models using Gaussian process regression on the Grassmann manifold, *Comput. Methods Appl. Mech. Eng.* 370 (2020) 113269. <https://doi.org/10.1016/j.cma.2020.113269>.
- [43] B. Bah, *Diffusion Maps : Analysis and Applications*, University of Oxford, 2008.
- [44] A. Olivier, D.G. Giovanis, B.S. Aakash, M. Chauhan, L. Vandanapu, M.D. Shields, UQpy: A general purpose Python package and development environment for uncertainty quantification, *J. Comput. Sci.* 47 (2020) 101204. <https://doi.org/10.1016/j.jocs.2020.101204>.
- [45] D. Lehmberg, F. Dietrich, G. Köster, H.-J. Bungartz, Datafold: Data-Driven Models for Point Clouds and Time Series on Manifolds, *J. Open Source Softw.* 5 (2020) 2283. <https://doi.org/10.21105/joss.02283>.
- [46] F. George, B.M. Golam Kibria, Confidence intervals for estimating the population signal-to-noise ratio: a simulation study, *J. Appl. Stat.* 39 (2012) 1225–1240. <https://doi.org/10.1080/02664763.2011.644527>.
- [47] L.F. Gabler, J.R. Crandall, M.B. Panzer, Development of a Metric for Predicting Brain Strain Responses Using Head Kinematics, *Ann. Biomed. Eng.* 46 (2018) 972–985. <https://doi.org/10.1007/s10439-018-2015-9>.
- [48] S.E. Davis, S. Cremaschi, M.R. Eden, Efficient Surrogate Model Development: Impact of Sample

Size and Underlying Model Dimensions, in: *Comput. Aided Chem. Eng.*, 2018: pp. 979–984. <https://doi.org/10.1016/B978-0-444-64241-7.50158-0>.

- [49] D.M. McGrath, N. Ravikumar, I.D. Wilkinson, A.F. Frangi, Z.A. Taylor, Magnetic resonance elastography of the brain: An in silico study to determine the influence of cranial anatomy, *Magn. Reson. Med.* 76 (2016) 645–662. <https://doi.org/10.1002/mrm.25881>.